Special Issue: RSS2021

The International Journal of Robotics Research
2023, Vol. 0(0) 1–15

DOI: 10.1177/02783649231188387
journals.sagepub.com/home/ijr

Optimizing contact patterns for robot locomotion via geometric mechanics

Baxi Chong[1], Tianyu Wang[1], Lin Bo[1], Shengkai Li[1], Pranav C. Muthukrishnan[1], Juntao He[1], Daniel Irvine[1], Howie Choset[2], Grigoriy Blekherman[1] and Daniel I. Goldman[1]

Abstract

Contact planning is crucial to the locomotion performance of robots: to properly self-propel forward, it is not only important to determine the sequence of internal shape changes (e.g., body bending and limb shoulder joint oscillation) but also the sequence by which contact is made and broken between the mechanism and its environment. Prior work observed that properly coupling contact patterns and shape changes allows for computationally tractable gait design and efficient gait performance. The state of the art, however, made assumptions, albeit motivated by biological observation, as to how contact and shape changes can be coupled. In this paper, we extend the geometric mechanics (GM) framework to design contact patterns. Specifically, we introduce the concept of "contact space" to the GM framework. By establishing the connection between velocities in shape and position spaces, we can estimate the benefits of each contact pattern change and therefore optimize the sequence of contact patterns. In doing so, we can also analyze how a contact pattern sequence will respond to perturbations. We apply our framework to sidewinding robots and enable (1) effective locomotion direction control and (2) robust locomotion performance as the spatial resolution decreases. We also apply our framework to a hexapod robot with two back-bending joints and show that we can simplify existing hexapod gaits by properly reducing the number of contact state switches (during a gait cycle) without significant loss of locomotion speed. We test our designed gaits with robophysical experiments, and we obtain good agreement between theory and experiments.

Keywords

Biologically inspired robots, geometric mechanics, contact planning, mechanism design and control, motion planning

Received 3 March 2022; Revised 4 March 2023; Accepted 19 June 2023

1. Introduction

In biological systems, animals properly coordinate their internal degrees of freedom (DoF) and their interactions with the environment to generate effective self-propulsion for stable and deliberate locomotion (Hildebrand, 1965, 1967; Kafkafi and Golani, 1998; Full and Koditschek, 1999; Ijspeert et al., 2007; Marvi et al., 2014; Astley et al., 2015). In legged and certain limbless systems body parts are properly sequenced to make and break contact with the environment in a way that achieves effective forward locomotion. Despite the advantages in making and breaking environmental contact, reproducing the capabilities of biological locomotors in robots is challenging; if not properly controlled, contact breaking can lead to unstable (Chong et al., 2021c) or uncoordinated (Marvi et al., 2014) locomotion.

Given the importance of contact pattern design, contact planning for robots has been extensively researched (Bouyarmane and Kheddar, 2012; Marvi et al., 2014; Astley et al., 2015; Gong et al., 2015; Aceituno-Cabezas et al., 2017; Chong et al., 2021c). A popular approach to contact pattern design is to take biological inspiration (Full and Koditschek, 1999) and use it to guide the robot locomotion control (Astley et al., 2015; Chong et al., 2021b; Astley et al., 2020). Another popular approach to contact pattern design is to use learning-based algorithms (Kohl and Stone, 2004; Gong et al., 2015; Carpentier et al., 2017; Hwangbo et al., 2019) to optimize contact patterns. While existing approaches have demonstrated their efficacy in various robots, little is known about the general principles behind contact planning. It remains unclear why certain contact patterns are effective and what happens if we perturb the contact pattern (e.g., delay the landing/lifting of

[1]Georgia Institute of Technology, Atlanta, GA, USA
[2]Carnegie Mellon University, Pittsburgh, PA, USA

Corresponding author:
Baxi Chong, Georgia Institute of Technology, 837 State Street NW, Atlanta, GA 30332, USA.
Email: bchong9@gatech.edu

some limbs or body segments). Understanding such principles can improve performance of the system, as well as the ability to derive new gaits based on the ones already determined.

Geometric mechanics has been developed as a general scheme to understand the principles behind seemingly complicated locomotion behaviors (Batterman, 2003; Kelly and Murray, 1995; Marsden, 1997; Ostrowski and Burdick, 1998; Shapere and Wilczek, 1989; Wilczek and Shapere, 1989). Specifically, the motion of a locomotion system is separated into a shape space (e.g., the internal joint angle space) and a position space (position and orientation of locomotor in the world frame). By establishing a mapping between velocities in shape and position spaces, geometric mechanics offers tools that allow us to visually analyze, design, and optimize gaits.

Recent efforts have extended geometric mechanics to mixed-contact systems (Chong et al., 2019, 2021b; Rieser et al., 2019). However, in such schemes the contact patterns are prescribed in the gait design process That is, the geometric tools are used to design the coordination between body posture changes and the prescribed contact patterns. As such, we cannot directly vary the contact patterns and evaluate how it should affect locomotion performance.

In this paper, we extend the geometric mechanics framework to design, analyze, and optimize contact patterns for robot locomotion. Specifically, we consider each contact state as an independent map connecting the shape space and position space. We then seek the optimal "switching" points between these maps that lead to the desired motion. Using the Hodge–Helmholtz theorem, which is explained in (Bhatia et al., 2012), we show that we can find the optimal transition points in the shape space. In the cases where there are more than three contact states, we prove that the contact sequence design problem can be reduced to a graph optimization problem (Schrijver, 2003, p. 114). We then apply our framework to design gaits for limbless and legged robots. We show that we can design effective sidewinding gaits for limbless robots with reduced spatial resolution (e.g., a 6-link limbless robot, Figure 1(a)). In addition, we show that we can modulate the heading[1] for a sidewinding limbless robot moving in an isotropic environment. Finally, we apply our contact sequence design framework to design gaits for an existing hexapod robot. Specifically, since most unstable behaviors in legged locomotion occur during contact switchs (Bai et al., 2019; Li et al., 2016), we use our framework to improve hexapod gaits by reducing the number of contact switches (within one period) without causing significant loss in locomotion performance. Our theoretical predictions are verified by robophysical experiments (Aguilar et al., 2016).

2. Background on geometric mechanics

In this section, we provide an overview of the geometric mechanics tools, which build the foundation of the framework introduced in this paper. For a more detailed and comprehensive review, we refer readers to Ostrowski and Burdick (1998); Marsden and Ratiu (2013); Gong et al. (2018); Hatton and Choset (2015); Zhong et al. (2018). The geometric mechanics gait design framework separates the configuration space of a system into two spaces: a position space and a shape space. The position space represents the location (position and rotation) of a system in the world frame, while the shape space denotes the internal shape of the system, for example, the joint angles. The geometric mechanics framework then establishes a functional relationship which maps velocities in the shape space to velocities in the position space; this functional relationship is often called the *local connection* (Hatton et al., 2013).

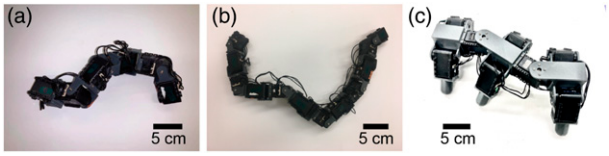

Figure 1. Robots with variable contact states: (a) A 6-link sidewinding limbless robot, (b) a 12-link sidewinding limbless robot, and (c) a hexapod robot with two body-bending joints.

2.1. Kinematic Reconstruction Equation

In kinematic systems where inertial effects are negligible, the equations of motion (Marsden and Ratiu, 2013) can be approximated as follows.

$$\boldsymbol{\xi} = \boldsymbol{A}(\boldsymbol{r})\dot{\boldsymbol{r}}, \tag{1}$$

where $\boldsymbol{\xi} = [\xi_x, \xi_y, \xi_\theta]^T$ denotes the body velocity in the forward, lateral, and rotational directions, respectively; $\boldsymbol{r}$ denotes the internal shape variables (joint angles); $\boldsymbol{A}(\boldsymbol{r})$ is the local connection matrix, which encodes environmental constraints and the conservation of momentum. While there has been research extending geometric mechanics to higher dimensions (Chong et al., 2019; Ramasamy and Hatton, 2016), the analysis and visualization power of geometric mechanics are particularly effective when the shape variable is 2-dimensional, that is, $\boldsymbol{r} \in \mathbb{R}^2$. In the applications where there are more than two joints (e.g., N degrees-of-freedom), we use two shape basis functions (Hatton et al., 2013) to reduce the dimensionality of the system. As reported in Gong et al. (2016), we can simplify the shape basis function by using a basis vector. To wit,

$$\boldsymbol{w} = [\boldsymbol{\beta}_1, \boldsymbol{\beta}_2]\boldsymbol{r},$$

where β_1 and β_2 are column vectors of shape basis functions. In the application to snake robots, prior work (Hatton et al., 2013; Gong et al., 2016) chose the shape basis functions to be:

$$\begin{aligned}\boldsymbol{\beta}_1(i) &= \sin\left(2\pi f_s \frac{i}{N-1}\right),\\ \boldsymbol{\beta}_2(i) &= \cos\left(2\pi f_s \frac{i}{N-1}\right), 1 \le i \le N\end{aligned} \tag{2}$$

where $\beta_m(i)$ is the i-th element of the vector β_m, f_s is the spatial frequency of the body undulation, i denotes the joint index, and N is the total number of joints.

2.2. Numerical derivation of local connection matrix

The local connection matrix $\boldsymbol{A}$ can be numerically derived using resistive force theory (RFT) to model the ground reaction force (Li et al., 2013; Sharpe et al., 2015; Zhang and Goldman, 2014; Hu et al, 2009). In this subsection, we provide a brief derivation of the local connection matrix needed for this paper.

The ground reaction force (GRF) experienced by the locomotor is the sum of the GRF experienced by each body segment. We assume that for each segment, the GRF acts on the center of the segment. RFT decomposes the resistive forces experienced by a body segment of a locomotor into two components: thrust (perpendicular) and drag (parallel), that is,

$$\boldsymbol{F} = \sum_{i \in I} \left(\boldsymbol{F}^i_{\parallel} + \boldsymbol{F}^i_{\perp}\right),$$

where $\boldsymbol{F}^i_{\parallel}$ and $\boldsymbol{F}^i_{\perp}$, respectively, denote forces parallel and perpendicular to the segment i; I is the collection of all the modules that are instantaneously in contact with the environment which we indicate using the following binary function, described in section 3.1., $I = \{i \mid c(i) = 1\}$. Note that here we assume the supporting forces/pressures are uniformly distributed among all the contacting segments. In many applications, the attack angle (the angle of body velocity with respect to the orientation of the body segment) determines the $\boldsymbol{F}_{\parallel}$ and $\boldsymbol{F}_{\perp}$ on this body segment, that is,

$$\boldsymbol{F}_{\parallel} = \boldsymbol{F}_{\parallel}(\chi), \boldsymbol{F}_{\perp} = \boldsymbol{F}_{\perp}(\chi),$$

where χ is the attack angle. $\boldsymbol{F}_{\parallel}$ and $\boldsymbol{F}_{\perp}$ are approximately independent of the magnitude of the velocity in granular and frictional systems (Zhang and Goldman, 2014). Depending on the substrate, we can choose the corresponding RFT functions to approximate the ground reaction forces.

The attack angles χ of each segment can be calculated from the body velocity $\boldsymbol{\xi}$, body shape $\boldsymbol{r}$, and shape velocity $\dot{\boldsymbol{r}}$ (Murray, 2017). Assuming damping overwhelms inertia, we consider the total net force applied to the system to be zero at any instance in time:

$$\boldsymbol{F} = \sum_{i \in I} \left[\boldsymbol{F}^i_{\parallel}(\boldsymbol{\xi}, \boldsymbol{r}, \dot{\boldsymbol{r}}) + \boldsymbol{F}^i_{\perp}(\boldsymbol{\xi}, \boldsymbol{r}, \dot{\boldsymbol{r}})\right] = 0. \tag{3}$$

At a given body shape $\boldsymbol{r}$, equation (3) connects the shape velocity $\dot{\boldsymbol{r}}$ to the body velocity $\boldsymbol{\xi}$. Therefore, by the implicit function theorem and the linearization process, we can numerically derive the local connection matrix $\boldsymbol{A}(\boldsymbol{r})$. In our implementation, we compute the solution of equation (3) using the MATLAB function *fsolve*.

2.3. Connection vector fields and height functions

Each row of the local connection matrix can be regarded as a vector field over the shape space, called the connection vector field. In this way, the body velocities in the forward, lateral, and rotational directions are computed as the dot product of connection vector fields and the shape velocity $\dot{\boldsymbol{r}}$. We focus here on the first row of the local connection matrix because it represents body velocity in the forward direction. This connection vector field is so named because it *connects* the shape variables $\boldsymbol{r}$ to the body velocity variable in the forward direction.

The displacement along the gait path $\partial\phi$ can be obtained by integrating the ordinary differential equation (Hatton and Choset, 2015) below:

$$g(T) = \int_{\partial\phi} T_e L_{g(r)} \boldsymbol{A}(\boldsymbol{r}) \mathrm{d}\boldsymbol{r}, \tag{4}$$

where $g(\boldsymbol{r}) = \begin{bmatrix} x(\boldsymbol{r}) \\ y(\boldsymbol{r}) \\ \theta(\boldsymbol{r}) \end{bmatrix}$ represents the position and rotation of body frame viewed in the world frame at position r (Murray, 2017), T is the time period of a gait cycle, and $g(T) = \begin{bmatrix} \Delta x \\ \Delta y \\ \Delta\theta \end{bmatrix}$ denotes the translation and rotation of the body frame (with respect to the world frame) in one gait cycle. Note that $T_e L_g$ is the left-lifted action with respect to the coordinates of g:

$$T_e L_g = \begin{bmatrix} \cos(\theta) & -\sin(\theta) & 0 \\ \sin(\theta) & \cos(\theta) & 0 \\ 0 & 0 & 1 \end{bmatrix}.$$

Each of the three integrals of equation (4) can be approximated to the first order as follows.

$$\begin{pmatrix} \Delta x \\ \Delta y \\ \Delta\theta \end{pmatrix} = \int_{\partial\phi} \boldsymbol{A}(\boldsymbol{r}) \mathrm{d}\boldsymbol{r} = \int_{\partial\phi} \begin{bmatrix} \boldsymbol{A}^x(\boldsymbol{r}) \\ \boldsymbol{A}^y(\boldsymbol{r}) \\ \boldsymbol{A}^\theta(\boldsymbol{r}) \end{bmatrix} \mathrm{d}\boldsymbol{r}, \tag{5}$$

where $\boldsymbol{A}^x$, $\boldsymbol{A}^y$, $\boldsymbol{A}^\theta$ are the three rows of the local connection, respectively. The accuracy of the approximation in equation (5) can be optimized by properly choosing the body frame (Hatton and Choset, 2015; Lin et al., 2020). According to Stokes' theorem, the line integral along a closed curve $\partial\phi$ is equal to the surface integral of the curl of $\boldsymbol{A}(\boldsymbol{r})$ over the surface enclosed by $\partial\phi$:

$$\int_{\partial\phi} \boldsymbol{A}(\boldsymbol{r}) \mathrm{d}r = \iint_{\phi} \nabla \times \boldsymbol{A}(\boldsymbol{r}) \mathrm{d}r_1 \mathrm{d}r_2, \tag{6}$$

where ϕ denotes the surface enclosed by $\partial\phi$. The curl of the connection vector field, $\nabla \times \boldsymbol{A}(\boldsymbol{r})$, is referred to as a

height function (or collectively as the constraint curvature functions, CCFs) (Hatton and Choset, 2015). The three rows of the local connection matrix $\boldsymbol{A}(\boldsymbol{r})$ can thus produce three height functions in the forward, lateral, and rotational directions, respectively.

With the above derivation, the gait design problem is simplified to drawing a closed path in the shape space. Net displacement over a period can be approximated by the integral of the surface enclosed by the gait path. Hence, the maximization of the integral leads to the maximization of displacement.

2.4. Effect of Drag Anisotropy

Locomotion effectiveness can be highly dependent on the ground reaction forces. Specifically, while terrestrial limbless robots can achieve good mobility on granular media using lateral undulation, they often struggle on frictional ground (Alben, 2019). To illustrate how the geometric approach provides insight into substrate dependence we compare the height function for an 8-link snake robot (with $f_s = 1.5$) moving on surface of a model granular media (poppy seeds) and frictional ground (Figure 2).

The ground reaction forces governing the interaction of body segments and granular media are well studied when moving on a granular surface. The forces $\boldsymbol{F}_\perp$ and $\boldsymbol{F}_\parallel$ (McInroe et al., 2016) can be approximated by:

$$f_\perp = C\sin(\chi), f_\parallel = A\cos(\chi) + B(1 - \sin(\chi)) + F_0,$$

where χ is the attack angle; $C = 0.66$, $A = 0.27$, $B = -0.32$, $F_0 = 0.09$ is the empirically fitted function to characterize the granular media resistance force (Aguilar et al., 2016; Schiebel et al., 2020). From the structure and magnitude of its height function (Figure 2(a)), we see that, with proper gaits, the robot can move effectively on granular media as discussed in Schiebel et al. (2020).

The ground reaction force between the body segments and the frictional ground can then be modelled by dry Coulomb kinetic friction:

$$f_\perp = f_0\sin(\chi), f_\parallel = f_0\cos(\chi),$$

where $f_0 = \mu F$ is the magnitude of the Coulomb kinetic friction, μ is the coefficient of friction, and F is the magnitude of the normal supporting force. The height function (Figure 2(b)) suggests that the robot has almost negligible speed regardless of the choices of gaits. However, it is important for limbless robots to move effectively on frictional ground. Inspired by sidewinding snakes (Marvi et al., 2014), limbless robots can greatly improve the maneuverability by properly controlling their contact patterns (Astley et al., 2015).

3. Contact scheduling

In the previous section where we modeled systems with continuous contact, we made an assumption that there is no change in contact states throughout the gait. This will be explained in section 3.1. In this section, we show that if we relax this assumption, we can greatly improve locomotor performance.

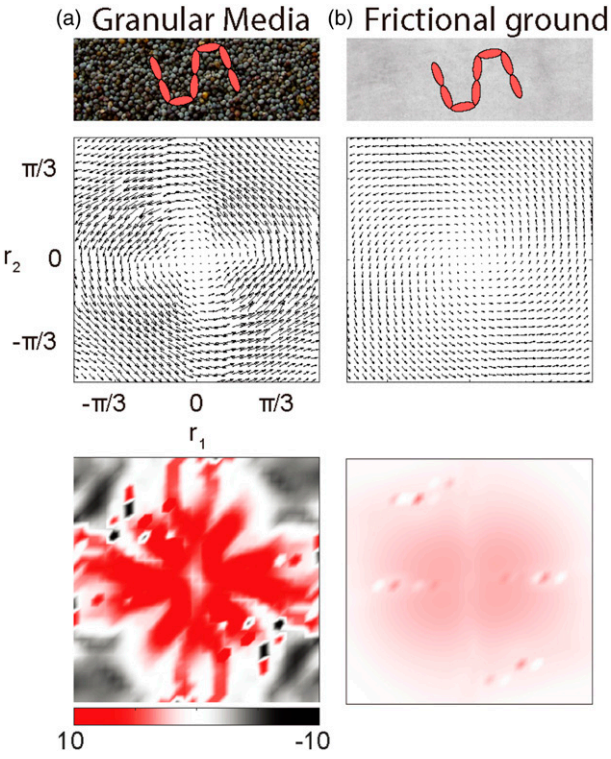

Figure 2. Vector fields and height functions for an 8-link robot on granular media and frictional ground with continuous contact. (a) A schematic sketch, vector field, and height function for an 8-link robot moving on granular media (poppy seeds). The height function has a large magnitude. (b) The sketch, vector field, and height function for an 8-link robot moving on frictional ground. The axes of all shape space are identical. The color bar of height functions in (a) and (b) is identical. The unit of the color bar in the height functions is BL/π2.

3.1. Single Contact State

Consider a 12-link limbless robot moving on frictional ground. We assign a binary variable to each link, $c(i)$, such that $c(i) = 0$ denotes link i in swing phase (no contact) and $c(i) = 1$ denotes link i in stance phase (full contact). As we will discuss below, the structure of the robot is such that $c(2i) = c(2i - 1)$ I = { i | c(i) = 1} (Chong et al., 2021c).

For illustration purpose, we consider three examples of contact states: I_1, I_2, and I_3:

Contact state	c (1) c (2)	c (3) c (4)	c (5) c (6)	c (7) c (8)	c (9) c (10)	c (11) c (12)
I_1	1	0	1	1	0	1
I_2	1	1	0	1	1	0
I_3	0	1	1	0	1	1

Note that none of these contact states are dependent on $\boldsymbol{r}$. Their realizations can be visualized in Figure 3(a)-(c). For

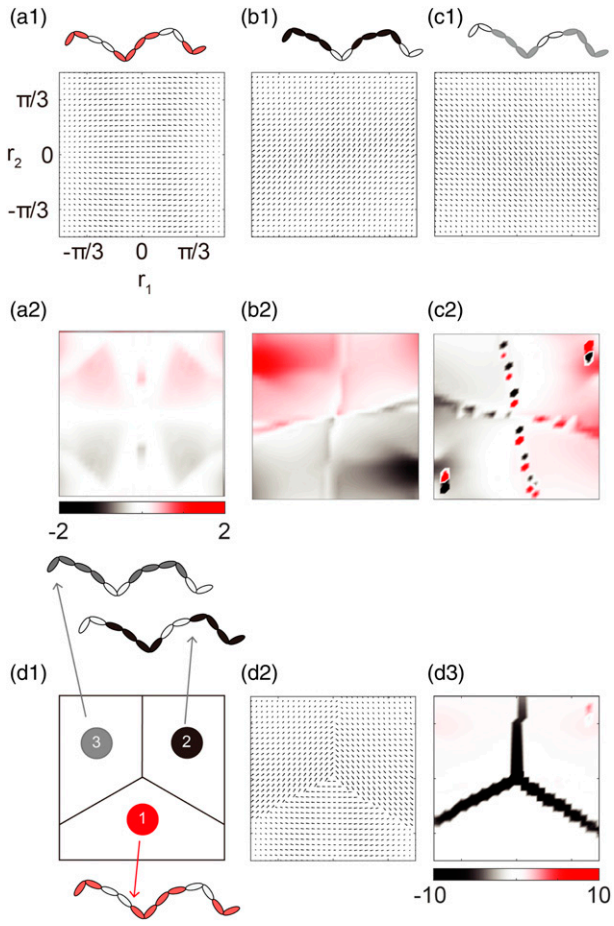

Figure 3. Example of a mixed contact pattern. (a)–(c) The vector fields and height functions for three contact states I1, I2, and I3. Corresponding robot links which are in contact with the environment are denoted by red, black, and grey. The color bars of height functions in (a), (b), and (c) are identical. (d.1) The contact pattern prescribed by equation (7). (d.2) The vector field prescribed by equation (8). (d.3) The corresponding height function. The axes of all shape space are identical. The unit of the color bar in all height functions is BL/π2.

each contact state, we compute its vector field and height function in the lateral direction (Figure 3(a)-(c)). We observe that in all cases, the height functions do not have regular patterns and their magnitude is low, which indicates limited mobility when a limbless robot uses a single contact state.

3.2. Mixed contact state

Although each individual contact state cannot lead to effective displacement, previous work demonstrated that their combination can enable new motion behaviors. In this section, we evaluate the locomotion performance of mixed contact states. For example, we construct the contact state as follows.

$$(r_1,r_2)\begin{cases} I_1 & \text{if } \operatorname{atan2}(r_2,r_1) \in (7\pi/6, 11\pi/6] \\ I_2 & \text{if } \operatorname{atan2}(r_2,r_1) \in (\pi/2, 7\pi/6] \\ I_3 & \text{if } \operatorname{atan2}(r_2,r_1) \in (-\pi/6, \pi/2] \end{cases}. \quad (7)$$

where atan2 is the four-quadrant inverse tangent operator. In this way, we can rewrite the local connection as follows.

$$(r_1,r_2)\begin{cases} \boldsymbol{A}_1 & \text{if } \operatorname{atan2}(r_2,r_1) \in (7\pi/6, 11\pi/6] \\ \boldsymbol{A}_2 & \text{if } \operatorname{atan2}(r_2,r_1) \in (\pi/2, 7\pi/6] \\ \boldsymbol{A}_3 & \text{if } \operatorname{atan2}(r_2,r_1) \in (-\pi/6, \pi/2] \end{cases}. \quad (8)$$

Its realization is shown in Figure 3(d.1). We then obtain the vector field and height function using equation (7); these are shown in Figure 3d (2-3). Interestingly, the new height function has substantially higher magnitude than constant contact height functions in Figure 3(a-c)2, and exhibits regular patterns (dark region along the boundary).

3.3. Optimal contact scheduling

Note that equation (7) is manually designed, inspired by biology and empirical experience (Astley et al., 2015; Rieser et al., 2019; Astley et al., 2020). Thus, the optimality of equation (7) remains unclear. To explore the optimization of contact patterns, we formulate the following optimization problem. To simplify our problem, we limit the number of contact states to 3. Note that the first row (called the A^x-component) of the local connection in equation (8) defines a discontinuous vector field on shape space. Moreover, the restriction on the polar angle of points (r_1, r_2) defines a partition of the shape space M. Let

$$\begin{aligned} M_1 &= \{(r_1,r_2)\in M | \operatorname{atan2}(r_2,r_1)\in(7\pi/6, 11\pi/6]\}\cup\{(0,0)\} \\ M_2 &= \{(r_1,r_2)\in M | \operatorname{atan2}(r_2,r_1)\in(\pi/2, 7\pi/6]\}\backslash\{(0,0)\} \\ M_3 &= \{(r_1,r_2)\in M | \operatorname{atan2}(r_2,r_1)\in(-\pi/6, \pi/2]\}\backslash\{(0,0)\} \end{aligned}.$$

By construction, every point of the shape space M lies in precisely one of the sets M_1, M_2 or M_3.

Next we explain how to perform a contour integral, (5), of the discontinuous vector field $A^x(r_1, r_2)$ that is defined in formula (8) along the unit circle. Let $l = \partial D^2$ denote the unit circle in M, and note that the three intersections $l_i = l \cap M_i$ are each an arc of the unit circle of arc length $2\pi/3$. Let $\overline{l_i} = l \cap \overline{M_i}$ denote the closure of each arc. Then each pairwise intersection $\overline{l_i} \cap \overline{l_j}$ consists of a single point. Specifically,

$$\overline{l_1}\cap\overline{l_2} = (\cos(7\pi/6), \sin(7\pi/6)),$$

and so on. These intersection points will be important later when we apply the fundamental theorem of line integrals. We can now split up the contour integral (5) as follows

$$\Delta x = \int_l A^x(\boldsymbol{r})\mathrm{d}\boldsymbol{r} = \sum_{i=1}^{3}\int_{l_i} A_i^x(\boldsymbol{r})\mathrm{d}\boldsymbol{r}$$

We focus here only on Δx, but a similar computation can be performed for Δy and $\Delta\theta$. This example provides motivation for the following problem.

Problem 1. Given 3 vector fields $\boldsymbol{A}_1^x, \boldsymbol{A}_2^x, \boldsymbol{A}_3^x$ in a shape space M, let p be any partition $M = M_1^p \cup M_2^p \cup M_3^p$ such that each subset M_i^p has positive volume. Define a discontinuous vector field A_p^x on M by the following formula

$$\boldsymbol{A}_p^x(\boldsymbol{r}) = A_i^x(\boldsymbol{r}) \text{ if } \boldsymbol{r} \in M_i^p.$$

Let L^p be the set of closed loops l in M such that for $i = 1, 2, 3$, the intersection $l \cap M_i^p$ is connected and simply connected. We wish to optimize

$$\max_{l,p} \oint_l \boldsymbol{A}_p^x(\boldsymbol{r}) \mathrm{d}\boldsymbol{r} \forall l \in L^p$$

where the maximum is taken over all loops l in L^p and over all partitions of M.

Since each region $l \cap M_i^p$ is connected and simply connected, we may define the following:

$$\begin{array}{llllll} l_1 & = l \cap \overline{M_1^p}, & l_2 & = l \cap \overline{M_2^p}, & l_3 & = l \cap \overline{M_3^p}, \\ \{q_\beta\} & = l_1 \cap l_3, & \{q_\gamma\} & = l_1 \cap l_2, & \{q_\alpha\} & = l_2 \cap l_3, \end{array} \tag{9}$$

where the overline denotes the closure of a set. We do not decorate l_i with overlines, so as to keep the notation simple. Then

$$\oint_l \boldsymbol{A}_p^x(\boldsymbol{r}) \mathrm{d}\boldsymbol{r} = \sum_{i=1}^{3} \int_{l_i} A_i^x(r_1, r_2) \mathrm{d}\boldsymbol{r}. \tag{10}$$

Note that in equation (10), each component is path-dependent, which is not desirable. From the Hodge–Helmholtz theorem, any vector field can be decomposed into the sum of a curl-free component, $(\boldsymbol{A}_1^x)_c$, and a divergence-free component, $(\boldsymbol{A}_1^x)_d$. In other words,

$$\boldsymbol{A}_1^x = \left(\boldsymbol{A}_1^x\right)_c + \left(\boldsymbol{A}_1^x\right)_d.$$

Note that in our applications, the curl-free component has a much greater magnitude than the divergence-free component (Figure 4(a)). Therefore, we approximate the line integral in the original vector field by the line integral in the curl-free component from the Hodge–Helmholtz decomposition. Note that in the case where the divergence-free component has comparable magnitude as the curl-free component, we can use the divergence-free components to determine the paths connecting the intersections once we determine the partition.

For curl-free vector fields, the line-integral is path-independent. Suppose, the corresponding potential functions of the curl-free components are P_1^x, P_2^x, P_3^x, respectively. These potential functions are graphed in Figure 4(b). By the fundamental theorem of line integrals, we have

$$\int_{l_1} \boldsymbol{A}_1^x(r_1, r_2) \mathrm{d}\boldsymbol{r} \approx \int_{l_1} \left(\boldsymbol{A}_1^x\right)_c (r_1, r_2) \mathrm{d}\boldsymbol{r} = P_1^x(q_\beta) - P_1^x(q_\gamma).$$

The approximation comes from the fact that the curl-free component of the connection vector field (in isotropic environments) dominates over the divergence-free

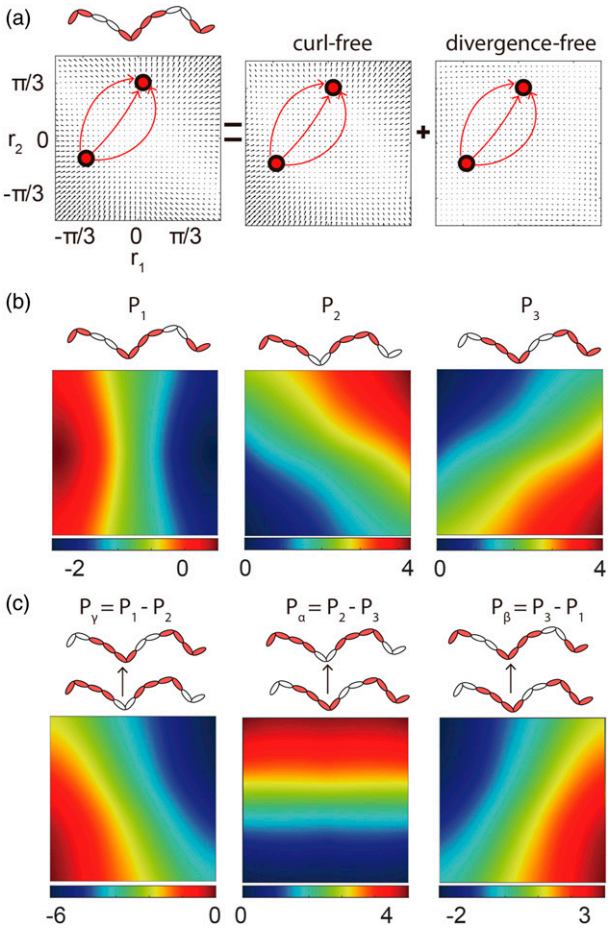

Figure 4. Illustration of a contact pattern optimization. (a) The vector field and its curl-free component and divergence-free component by the Hodge–Helmholtz decomposition. (b) The potential functions for P_1, P_2, and P_3. Note that in curl-free components, the line integral is path-independent, allowing us to compute the potential function to estimate the line integral between any points. (c) The potential function difference for $P_\gamma = P_2 - P_1$, $P_\alpha = P_3 - P_2$, and $P_\beta = P_1 - P_3$. The axes of all shape spaces are identical. The unit of the color bar in all potential function differences is BL/π2.

component. The other two terms in (10) are decomposed similarly. Then our objective function becomes

$$\begin{aligned} \oint_l \boldsymbol{A}(\boldsymbol{r}) \mathrm{d}\boldsymbol{r} &\approx \left(P_1^x(q_\beta) - P_1^x(q_\gamma)\right) + \left(P_2^x(q_\gamma) - P_2^x(q_\alpha)\right) \\ &\quad + \left(P_3^x(q_\alpha) - P_3^x(q_\beta)\right) \\ &= \left(P_3^x - P_2^x\right)(q_\alpha) + \left(P_1^x - P_3^x\right)(q_\beta) \\ &\quad + \left(P_2^x - P_1^x\right)(q_\gamma) \\ &= P_\alpha^x(q_\alpha) + P_\beta^x(q_\beta) + P_\gamma^x(q_\gamma), \end{aligned} \tag{11}$$

where $P_\alpha^x := P_3^x - P_2^x$, $P_\beta^x := P_1^x - P_3^x$, and $P_\gamma^x := P_2^x - P_1^x$ are the potential function differences (PFDs) (Figure 4(c)). Note that our objective function has separated parameters—the coordinates of $q_\alpha, q_\beta, q_\gamma$. In addition, the choices of partition and l imply that all three

intersection points could be arbitrary points in M. As a result, when (11) is optimized, so are the three individual terms in (11). Therefore, q_α is the point in M that optimizes the univariate function P^x_α. Parameters q_β, q_γ are characterized similarly.

Since the vector fields $\boldsymbol{A}^x(r)$ are given, so are the PFDs $P^x_\alpha, P^x_\beta, P^x_\gamma$. Thus, we can find the optimal contact scheduling by solving these three individual optimization problems. In practice, if we discretize the values of $P^x_\alpha, P^x_\beta, P^x_\gamma$, we can apply numerical algorithms to solve these optimization problems.

Once q_α, q_β, q_γ are found, we can then choose a generic point q_0 in M. For convenience, let q_0 be the origin. Choose a curve connecting q and q_α to $\overline{M^p_2} \cap \overline{M^p_3}$. The other two boundaries are obtained by connecting and extending q, q_β and q, q_γ, and we obtain the partition p, which leads to the optimal contact scheduling.

3.4. Applications to more than three contact states

Our methods can be applied to systems with more than three states. In practice, however, it is surprisingly challenging to directly applying our methods to systems with more than three contact states.

3.4.1. NP-hardness. Consider a locomotion system with multiple contact states I. We construct a weighted-directed complete graph $G(V, E)$, where vertices $v_i \in V$ correspond to contact states $I_i \in I$, and the edge from v_i to v_j has weight w_{ij}, as the cost to transit from contact state I_i to contact state I_j. From our previous analysis, the edge weight w_{ij} can be approximated by the maximum value in the potential function difference $(P^i - P^j)$, which we can numerically calculate.

To find the optimal contact sequence and the associated shape changes, we need to find a cycle C passing each of the n vertices exactly once, such that the sum of weights along C is maximal. This is a special case of the *longest path problem*, which is NP-hard because of the NP-hardness of the Hamiltonian cycle problem (Schrijver 2003, p. 114).

Constraints. Solving the longest path problem, we may obtain an optimal cycle C and a corresponding loop in the shape space. However, in many cases, such paths can be considered as "multiple-period-gaits."

In our framework, we seek to maximize the displacement within *one* period. In other words, a gait is defined as a closed curve in the shape space, M, defined on an interval $[0, T]$. The set of all gaits is defined as follows

$$\Psi = \left\{ \psi \in C^1 \;\middle|\; \psi : [0, T] \to M, \psi(0) = \psi(T) \right\} \qquad (12)$$

Following this definition, the trajectories in Figures 5a and 5(b) are both considered as gaits. However, the gait in Figure 5(a) has an unfair advantage over the gait in Figure 5(b) because the blue path winds around the origin twice in one period, which takes two periods for the red path. Thus, the blue path should be penalized by dividing by the winding number. For simplicity, we only consider gaits that are simple closed curves. Thus, we define a gait to be a "multiple-period-gait" if it is non-simple.

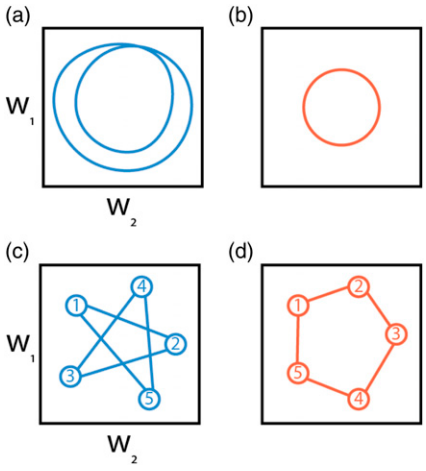

Figure 5. Example of multiple-period-gaits: (a) An example of a "multiple-period-gait" path in the shape space. (b) An example of a normal gait path in the shape space. (c)The transitional points (from 1 to 5) are placed such that they wind the origin more than once. It is considered as a multiple-period-gait in practice. (d) An example of a single-period-gait generated by connecting the transitional points.

Such "multiple-period-gaits" could be intentionally avoided if we directly design the trajectory in the shape space. However, when the gait design is abstracted to a graph $G(V, E)$, it is challenging to include such constraints in the optimization. In Figure 5(c), we show an example of "multiple-period-gait" trajectory and the transitional points.

Initialization by empirical gaits. While it is challenging to directly apply our methods to systems with more than three contact states, our framework can still offer insights into the analysis of these problems. For example, instead of solving the contact design by brute-force, we can start with an empirically derived gait and check (1) if the empirical gait is already at the local optimum and (2) if we can further improve this empirical gait.

4. Results

4.1. Experimental setup

Limbless robot. We carried out robophysical experiments with a modular limbless robot composed of identical modules actuated by Dynamixel AX-12A servo motors (Figures 1(a) and 1(b)). The number of modules varied according to the gait tested, but the arrangement of modules always followed the convention that the rotation axes of two neighboring modules were perpendicular to each other. Thus, all rotation axes of odd modules lie in the same plane

and the same is true for even modules. In experiments, odd modules were actuated to control the body shape in the horizontal plane and even modules were for the vertical plane.

4.1.1. Hexapod robot. We also validated our method on a hexapod robot with two rotational degrees of freedom in the body and one rotational degree of freedom in each leg (Figure 1(c)). The 30-cm-long elongated body is segmented by two bending joints which allows ±90 degrees of rotations. Each segment of the body is equipped with two legs on both sides, and lifting and landing of the leg are controlled by the rotational joint at the shoulder. All rotational joints of the robot are actuated by Dynamixel AX-12A servo motors. The body of the robot can be lifted up to 5 cm above the landing surface of feet.

4.1.2. Robot Experiment. Experiments were conducted on flat, frictional ground, with the assumption that the ground reaction forces can be modelled by dry Coulomb kinetic friction with friction coefficient $\mu = 0.35 \pm 0.06$ (between the plastic body and the frictional ground). The joints of the robot were controlled by direct joint angle set-point commands. We conducted three repeat experiments for each gait we tested. In a single experiment, the robot executed three complete gait cycles.

To track the robot's motion in its position space, six IR reflective markers were attached along the body of the robot with equal distance along the body. An OptiTrack motion capture system with six OptiTrack Flex 13 cameras was used. 3D positions of the markers were tracked at a frame rate of 120 FPS. The motions of the robot executing three gait cycles were collected from when the robot formed the first configuration until the robot reached the last configuration.

We measured the angle of motion and displacement from the robot motion data we collected. To calculate the angle of motion for one experiment (3 complete gait cycles), we selected the first and the last sets of marker positions, which correspond to the initial and the ending robot configurations, respectively. We then calculated the average geometric center of the body for two configurations by taking the mean of the position of markers. Thus, the trajectory of the geometric center in the world frame can be determined by connecting the starting and ending geometric centers. Similarly, the angle of motion can be measured by the angular difference between the geometry center trajectory and the horizontal axes (perpendicular to the starting body axis). The displacement can also be measured by the projection of the geometric center trajectory onto the horizontal axes.

4.2. Modulating sidewinding angle of motion

In previous work (Astley et al., 2015; Chong et al., 2021c), the sidewinding gait for limbless robots was decomposed into two waves, one in the horizontal plane and one in the vertical plane. In this way, the formulas of shape changes are prescribed as follows:

$$\theta(2j-1,t) = A_h \sin\left(2\pi K \frac{2j-1}{N} + 2\pi f t\right) \tag{13}$$

$$\theta(2j,t) = A_v \sin\left(2\pi K \frac{2j}{N} + 2\pi f t + \phi_0\right) \tag{14}$$

where $j = 1, 2, \ldots, N/2$; $\theta(2j-1, t)$ and $\theta(2j, t)$ refer to the yaw joint angles and the pitch joint angles, respectively; K is the spatial frequency of the sidewinding gaits; A_h and A_v are the amplitudes of the horizontal wave and the vertical wave, respectively; f defines the temporal frequency; and ϕ_0 is the phase lag between the horizontal and the vertical waves.

Rieser et al. (2019) showed that the track angle (the angle between the direction of motion and the trajectories of the "tracks" made by body–environment contact) can be modulated by the amplitude of the horizontal wave, A_h. On granular media, the measurement of track angle can give an approximation to the angle of motion (the angle between the direction of motion and the central axis of snake body). However, with our analysis in (4), the net displacement of sidewinding gaits on frictional ground is predominantly in the lateral direction.

We tested the sidewinding gaits with a range of amplitudes of the horizontal wave A_h, from 20 to 60 degrees, on a 12-link limbless robot moving on frictional ground. We found through experiments that the angle of motion is almost independent of the amplitude (Figure 6(a)). Example experiment videos for $A_h = \pi/3$ and $\pi/9$ can be found in the supplementary video. Given the low effectiveness of altering the horizontal amplitude on the motion angle modulation, we sought to design a general control scheme that would modulate this angle of motion in isotropic environments.

We applied our method to design sidewinding gaits for a 12-link robot and explore modulating the angle of motion. Following the method introduced in Sec. II, we computed the potential function difference in the forward, lateral, and rotation directions (Figure 7). Note that the shape basis function (equation (2)) and contact states (Table in Sec. 3.1) are subject to our choice. In concurrent work, we illustrate that further optimization can be conducted without manual choice of shape basis function or contact states (Chong et al., 2023). We identified the three transitional points that maximized the displacement in lateral directions, $Q^y = \{q^y_\alpha, q^y_\beta, q^y_\gamma\}$. Note that we limited the joint angle to $\pi/3$, that is, $\|[r_1, r_2]\|_2 < \pi/3$. We then identified the three transitional points that maximized the displacement in forward direction, $Q^x = \{q^x_\alpha, q^x_\beta, q^x_\gamma\}$. We observed that the transitional points Q^y can only lead to pure translation (i.e., zero in forward and rotational directions). Furthermore, the transitional points determined by Q^x can lead to effective displacement in both forward and lateral directions and thus establish a finite angle. In this way, we propose to modulate the angle of motion by a convex combination of Q^y and Q^x:

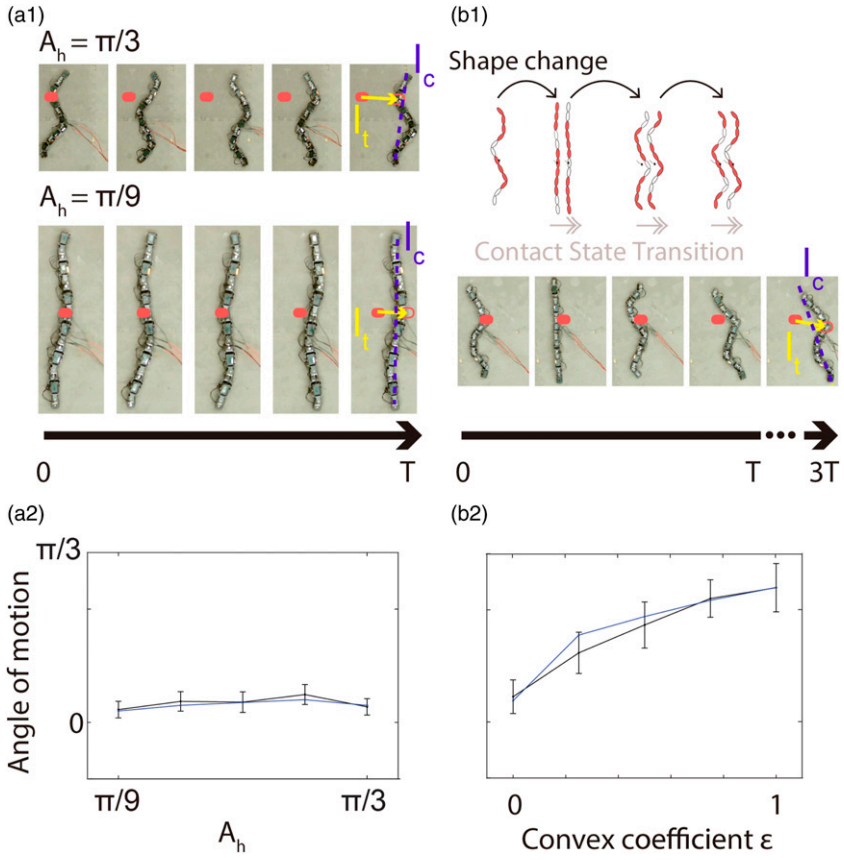

Figure 6. Experiments on angle of motion modulation. (a.1) Snapshots of a robot implementing sidewinding gaits with different amplitudes using sinusoidal templates (equations 13, and 14). Solid yellow arrow indicates the direction of motion l_t and dashed blue line lc indicates the central body axis. The angle between l_c and l_t is then defined as the angle of motion. (a.2) For the sidewinding gaits using sinusoidal templates, the angle of motion is almost independent of the amplitude for robot moving in isotropic environments. Blue solid line represents simulation, and black line with error bars is robophysical experimental data. (b.1) Comparison of snapshots of the robot experiment and the simulation implementing the gait to modulate the angle of motion. (b.2) Modulation of the motion angle by controlling the convex coefficient ε.

$$Q(\epsilon) = \epsilon Q^x + (1 - \epsilon)Q^y \tag{15}$$

where $\epsilon \in [0, 1]$ is the coefficient of the convex combination and $Q(\epsilon)$ are the transition points determined by the convex coefficient ϵ.

In this way, using equation (15), we formulated an equation to modulate the angle of motion. As shown in Figure 6(b), data from robophysical experiments agreed with our predictions, verifying the validity of our theoretical approach (an example robophysical experiment video can be found in the supplementary video). As such, we have shown that our method is effective in modulating the angle of motion for limbless sidewinding robots in isotropic environments.

4.3. Sidewinding of a 6-link Robot

In certain applications such as search and rescue in obstacle-rich environments, it could be desirable to have limbless robots with short body length but high locomotive performance in sidewinding. However, there is often a trade-off between the body length and the locomotive performance for limbless robots: if the size of the motor in each module is fixed, it is only possible to reduce the size of the robot by decreasing the number of motors, that is, decreasing the degrees of freedom. The disadvantage of fewer motors can be slower locomotion speed. As shown in Maladen et al. (2011), even when executing the same gait, robots with few motors have lower speed in granular swimming than those with more motors.

We conducted a series of experiments using the same motion equations but different number of motors. Specifically, we fixed the parameters $A_h = \pi/3$, $A_v = \pi/9$, $K = 1.5$, and $f = 0.1$ and evaluated the relationship between the speed and the number of motors, N. The experimental results are shown in Figure 8. As expected, the displacement decreased as the number of motors decreased until $N = 10$. Turning behavior emerged at $N < 10$, which can be caused by the unstable configurations in the gaits (Chong et al., 2021c). These unstable turning behaviors led to high variability in speed. An example of the unstable turning behavior for $N = 6$ can be found in the supplementary video.

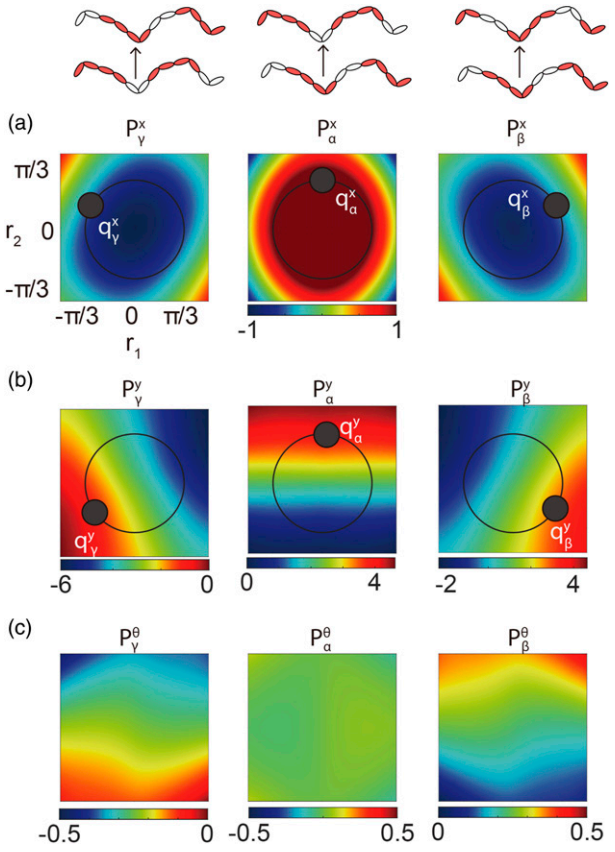

Figure 7. Modulating the angle of motion using contact pattern optimization. The potential function difference (PFD) in forward (a), lateral (b), and rotational (c) directions. The black circles indicate our joint angle limit: $\|[r_1, r_2]\|_2 \leq \pi/3$. The set of extreme points ($Q^x = \{q^x_\gamma, q^x_\alpha, q^x_\beta, \}$) are chosen to maximize the sum of PFD in forward directions. The set of extreme points ($Q^y = \{q^y_\gamma, q^y_\alpha, q^y_\beta, \}$) are chosen to maximize the sum of PFD in lateral directions. The axes of all shape spaces are identical. The color bar of PFD in (a) is identical. The unit of the color bar in all PFDs is BL/π^2.

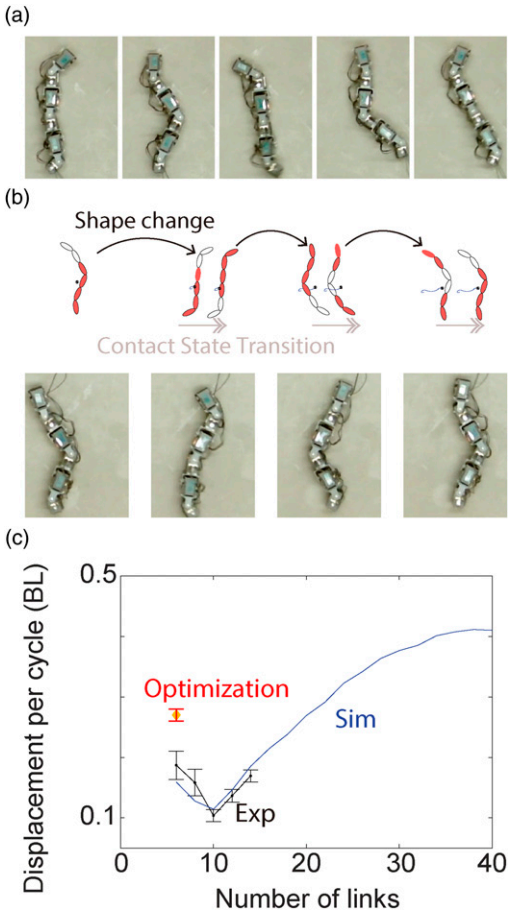

Figure 8. Sidewinding with few links. (a) Snapshots of a 6-link robot implementing the sidewinding gait with the sinusoidal templates (equation (13) and (14)). (b) Snapshots of a 6-link robot implementing the sidewinding gait with our optimization method. (c) The sidewinding speed (in unit BL per cycle) as a function of link numbers (sidewinding gait is prescribed using the sine wave template). Blue solid line represents simulation, and black line with error bars is robophysical experimental data. The speed decreases as the link number decreases until $N = 10$. For $N < 10$, the configuration is unstable and turning emerged. The speed of the gait with our optimization method is highlighted as a diamond marker.

We then used our method to design effective sidewinding gaits for the 6-link robot. We first identified three stable contact patterns for this 6-link robot such that the center of mass is enclosed by the supporting polygon. Using the methods introduced in Sec. II, we obtained the potential function difference in lateral direction (P^y_γ, P^y_α, and P^y_β) and rotational directions (P^θ_γ, P^θ_α, and P^θ_β). Interestingly, we noticed that the magnitude of P^y_β is significantly lower than those in P^y_γ and P^y_α. Therefore, the lateral speed is almost independent of the choice q_β; and given q_γ and q_α, we are free to choose q_β such that the net rotation is zero.

Given the transitional points, we interpreted the boundary of these contact states as the half line connecting origin and chosen transitional points. We then computed the corresponding vector field and height function.

We implemented our designed gaits in robot experiments. The experimental data shows quantitative agreement with the theoretical predictions. An example video of the 6-link robot experiment can be found in the supplementary video. Interestingly, we noticed that with proper design of the contact pattern, the speed of 6-link robot can even outperform a robot with 12 links (Figures 8(c) and 9).

4.4. Application to legged robots

Consider a hexapod robot with two body-bending joint angles (Figure 1(c)). Each foot has two contact states: stance phase and swing phase. In this way, there are in total $2^6 = 64$ contact states for the hexapod robot. As discussed before, it is difficult to incorporate the winding number constraints into the abstracted Hamiltonian cycle optimization problem. Instead, we started from an empirical hexapod gait (duty factor = 0.5 and lateral phase shift = 2/3) (Chong et al.,

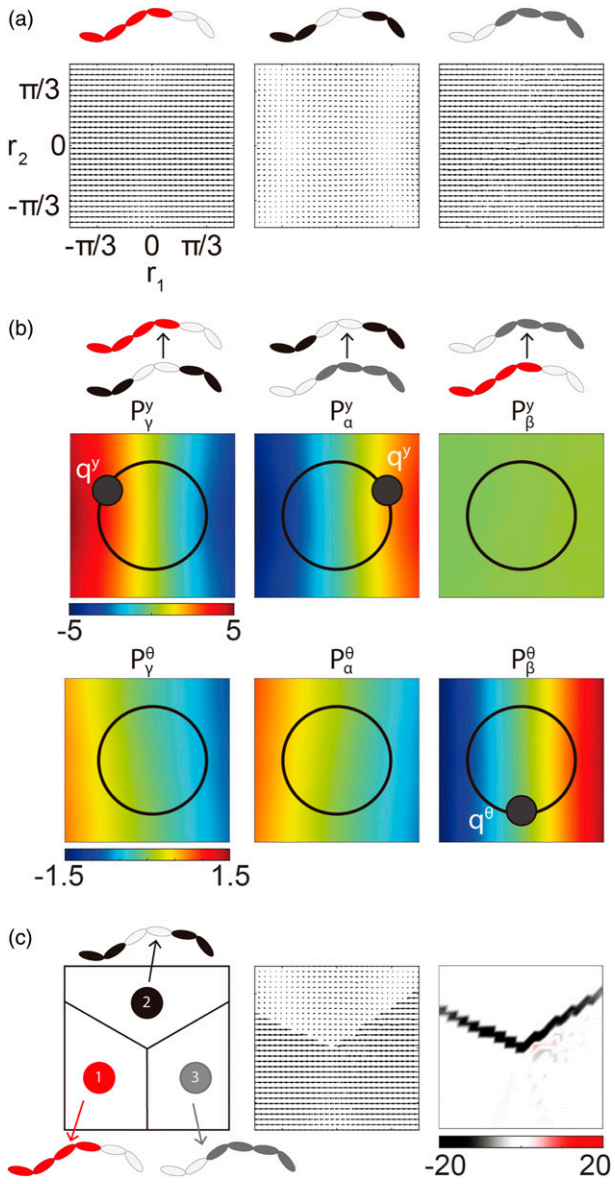

Figure 9. Designing sidewinding gaits for a 6-link robot. (a) Three stable contact patterns and their corresponding vector fields. (b) The PFD of lateral and rotational directions. The color bars of PFD are identical in three illustrations. The black circle indicates the robot's joint angle limit: $\|[r_1, r_2]\|_2 \leq \pi/3$. (c) The boundary of each contact state, the vector field, and the height function with the optimal contact pattern, determined from the obtained transitional points. The unit of color bar in height function is BL/π^2.

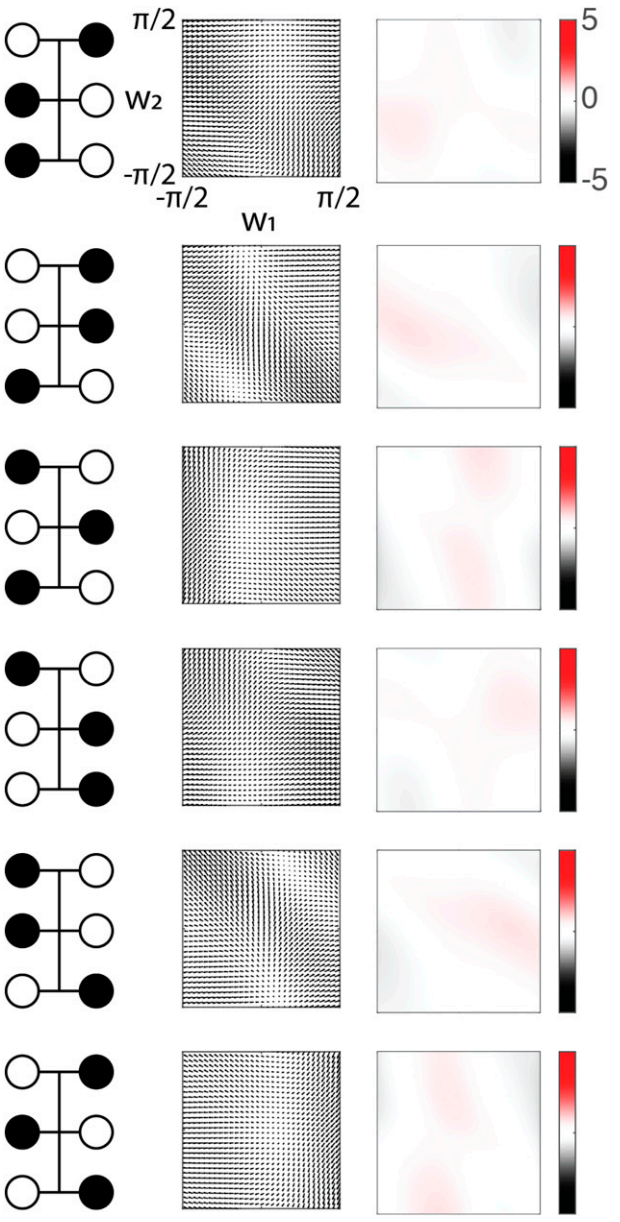

Figure 10. Contact states, vector fields, and height functions for a hexapod robot. The contact states from the empirical gait (left). The (almost curl-free) vector field corresponds to the contact state (middle). The height function associated with the contact states (right). The shape space has the same axis and color bar as labeled in the first row. The unit of color bar in the height function is BL/π^2.

2022) and checked if this empirical gait is a local optimum, or whether we could further improve the locomotion performance. The robophysical model implementing the empirical gaits is shown in Figure 11.

In the empirical gait, there are six contact states (Figure 10). Consider a shape space composed by w_1 (the upper body bending joint angle) and w_2 (the lower body bending joint angle); the connection vector field for each contact state is almost curl-free, leading to the low magnitude on the height function. In the empirical gait, these six contact states are properly sequenced and placed in the shape space. The new vector field (by partitioning from six vector fields) is shown in Figure 12(a). The new vector field therefore has a large curl, leading to a large magnitude in the height function.

We used our framework to evaluate whether the transitions of empirical gaits are local optima. We computed the corresponding potential function difference for each contact state transition and labeled the transitional points with black stars. We notice that for each contact state transition, there exists a range of shape positions where the contact

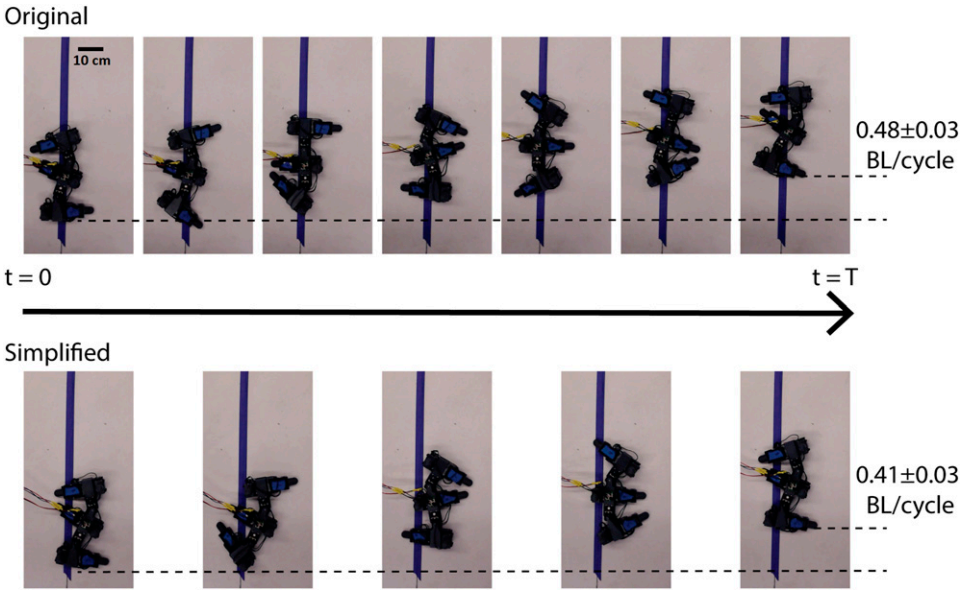

Figure 11. Robophysical model implementing the empirical and simplified hexapod gaits (top). Snapshots of a robophysical model implementing original (top) and simplified (bottom) hexapod gaits. Note that there are six contact states in original gait and four in simplified gait. The displacements of two gaits per cycle are similar.

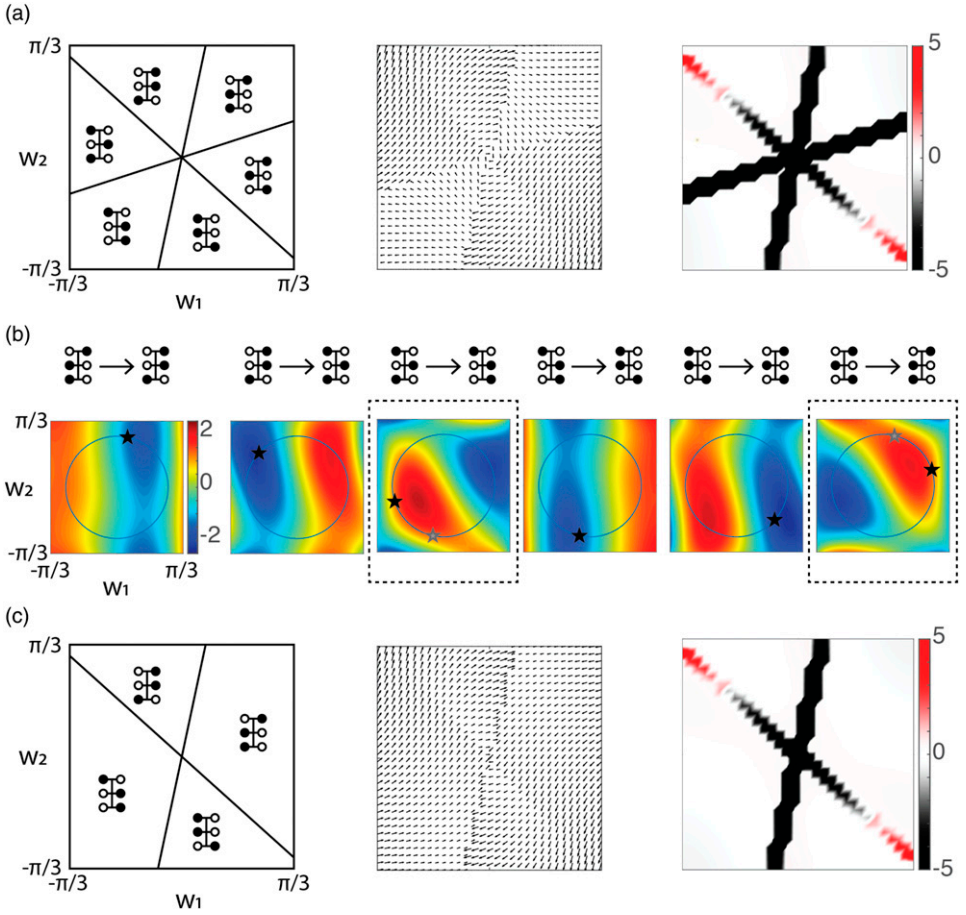

Figure 12. Simplifying the empirical hexapod gait. (a) The partition of the vector field from empirical gaits. Such partitioning can create a large curl in the vector field and thus have large magnitude in the height function. (b) The PFD for each contact state transition. Two out of six transitional points are non-optimal (labeled in the dashed box). The orange circle denotes the joint angle limit ($\pi/4$). The black star denotes the transitional points from the empirical gait. The grey star denotes the new location of non-optimal transitional points to create degenerate case. (c) The partition, vector field, and height function of simplified hexapod gait. The unit of color bar in all height functions and PFDs is BL/π^2.

switching state can be close to optimal (affecting less than 0.01 BL/cycle from the optima). Surprisingly, we noticed that only four out of six transitional points reside in the range of close-to-optimal (resulting in less than 0.01 BL/cycle compared to the optimum) contact switching shapes. We then proceeded to analyze whether we could improve the empirical gait by moving the non-optimal transitional points. We noticed that the local optima in PFD (Figure 12(d) dashed box) are far from the prior and posterior transitional points. Simply choosing the local optima as the transitional points can lead to problems such as self-intersection gait paths or gait paths with extremely large perimeters. To avoid these problems, we chose to move the non-optimal transitional points along their iso-height contours such that they collide with their posterior transitional points (labeled with grey stars). Notice that such sequenced gaits create a degenerate case where the intermediate contact states (Figure 12(b) dashed box) are essentially eliminated from the gaits. Since we move the transitional points along their iso-height contour, we expect the degenerate gait (with four contact states) will have similar locomotion performance as the original gait (with six contact states).

We verified our predictions by robophysical experiments. The snapshots of the robot implementing degenerate gait are shown in Figure 11. The robot experiments confirmed our prediction that the degenerate gait has similar locomotion performance as the original gait.

5. Conclusion

In this paper, we designed a framework to systematically optimize, analyze, and visualize the contact patterns that lead to limbless or legged robot locomotion in a desired direction. Specifically, we used a local connection to model each contact pattern, such a connection maps the velocities in the shape space to the position space. We then formulated the optimal contact pattern problem as finding the optimal boundary between each contact state in the shape space. Using the Hodge–Helmholtz theorem, we estimated the line integral in a vector field from its potential functions. By taking the difference in potential functions, we were able to search for global optimal transitional points in the shape space. Note that in the examples shown in the paper, the curl-free component has a much greater magnitude than the divergence-free component. In cases where the divergence-free and curl-free components have comparable magnitude, we can first determine the transitional points from the curl-free components and design the trajectory connecting transitional points using the divergence-free components.

We first applied our framework to study sidewinding limbless robots. We used our methods to modulate the angle of motion for sidewinding robots moving in isotropic environments. Robophysical experiments verified that we could modulate the angle of motion by controlling the weights in convex combination ε. We then applied our method to design a sidewinding gait for a 6-link robot. We showed that with proper contact design, the 6-link robot could achieve speeds as high as those with larger numbers of links (e.g., a 12-link robot). In this way, we expand the family of sidewinding gaits to robots with fewer motors and therefore enables diverse effective limbless locomotors for different environments/tasks.

We also applied our framework to a legged robot (a hexapod robot with two body-bending joints). We showed that while it is surprisingly challenging to directly design gaits for systems with more than three contact states, we can use our framework to simplify and/or further optimize the existing gaits.

Extensions to our work include systematically using our methods to study systems with more than three contact states. It will include properly designing the physical constraints on the feasible gaits and developing efficient algorithms to obtain effective gaits.

Declaration of conflicting interests

The author(s) declared no potential conflicts of interest with respect to the research, authorship, and/or publication of this article.

Funding

The author(s) disclosed receipt of the following financial support for the research, authorship, and/or publication of this article: This study is supported by the Simons Foundation and National Science Foundation (Simons Foundation SFARI 594594) and Army Research Office (W911NF-11-1-0514).

ORCID iDs

Baxi Chong https://orcid.org/0000-0002-6187-4911
Tianyu Wang https://orcid.org/0000-0001-9012-838X
Bo Lin https://orcid.org/0000-0001-9120-3142
Daniel Irvine https://orcid.org/0000-0003-2721-5901

Note

1. Heading is the angle that the robot's displacement vector makes with respect to the axis of the robot's body.

References

Aceituno-Cabezas B, Mastalli C, Dai H, et al. (2017) Simultaneous contact, gait, and motion planning for robust multilegged locomotion via mixed-integer convex optimization. *IEEE Robotics and Automation Letters* 3(3): 2531–2538.

Aguilar J, Zhang T, Qian F, et al. (2016) A review on locomotion robophysics: the study of movement at the intersection of robotics, soft matter and dynamical systems. *Reports on Progress in Physics* 79(11): 110001.

Alben S (2019) Efficient sliding locomotion with isotropic friction. *Physical Review E* 99(6): 062402.

Alexander S (2003) *Combinatorial optimization: polyhedra and efficiency*. Berlin, Germany: Springer Science & Business Media, vol. 24.

Astley HC, Gong C, Jin D, et al. (2015) Modulation of orthogonal body waves enables high maneuverability in sidewinding

locomotion. *Proceedings of the National Academy of Sciences* 112(19): 6200–6205.

Astley HC, Rieser JM, Abdul Kaba, et al. (2020) Side-impact collision: mechanics of obstacle negotiation in sidewinding snakes. *Bioinspiration & Biomimetics* 15(6): 065005.

Bai L, Hu H, Chen X, et al. (2019) Cpg-based gait generation of the curved-leg hexapod robot with smooth gait transition. *Sensors* 19(17): 3705.

Batterman RW (2003) Falling cats, parallel parking, and polarized light. *Studies In History and Philosophy of Science Part B: Studies In History and Philosophy of Modern Physics* 34(4): 527–557.

Bhatia H, Norgard G, Pascucci V, et al. (2012) The Helmholtz-Hodge decomposition—a survey. *IEEE Transactions on visualization and computer graphics* 19(8): 1386–1404.

Bouyarmane K and Kheddar A (2012) Humanoid robot locomotion and manipulation step planning. *Advanced Robotics* 26(10): 1099–1126.

Carpentier J, Budhiraja R and Mansard N (2017) Learning feasibility constraints for multi-contact locomotion of legged robots. In *Robotics: Science and Systems* RSS 2017: p 9.

Chen L, Zhang T and Goldman DI (2013) A terradynamics of legged locomotion on granular media. *Science* 339(6126): 1408–1412.

Chong B, Aydin YO, Sartoretti G, et al. (2019) A hierarchical geometric framework to design locomotive gaits for highly articulated robots *Robotics: Science and Systems*. RSS 2019.

Chong B, Aydin YO, Rieser JM, et al. (2022) A general locomotion control framework for multi-legged locomotors. *Bioinspiration & Biomimetics* 17(4): 046015.

Chong B, Aydin YO, Gong C, et al. (2021b) Coordination of lateral body bending and leg movements for sprawled posture quadrupedal locomotion. *The International Journal of Robotics Research* 40: 0278364921991158.

Chong B, Wang T, Rieser JM, et al. (2021c) Frequency modulation of body waves to improve performance of sidewinding robots. *The International Journal of Robotics Research* 40: 02783649211037715.

Chong B, Luo D, Wang T, et al. (2023) Geometry of contact: contact planning for multi-legged robots via spin models duality. *arXiv preprint arXiv:2302.03019*, 2023. https://arxiv.org/abs/2302.03019

Frank W and Shapere A (1989) *Geometric phases in physics*. Singapore: World Scientific, vol. 5.

Full RJ and Koditschek DE (1999) Templates and anchors: neuromechanical hypotheses of legged locomotion on land. *Journal of Experimental Biology* 202(23): 3325–3332.

Gong C, Travers M, Astley HC, et al. Limbless locomotors that turn in place. In 2015 *IEEE International Conference on Robotics and Automation (ICRA)*. NY, USA: IEEE pages 3747–3754, 2015.

Gong C, Goldman DI and Choset H (2016) Simplifying gait design via shape basis optimization. In *Robotics: Science and Systems*, RSS 2016.

Gong C, Whitman J, Grover J, et al. (2018) Geometric motion planning for systems with toroidal and cylindrical shape spaces. In *Dynamic Systems and Control Conference*, DSCC 2018.

Hatton RL and Choset H (2015) Nonconservativity and noncommutativity in locomotion. *The European Physical Journal Special Topics* 224(17-18): 3141–3174.

Hatton RL, Ding Y, Choset H, et al. (2013) Geometric visualization of self-propulsion in a complex medium. *Physical Review Letters* 110(7): 078101.

Hildebrand M (1965) Symmetrical gaits of horses. *Science* 150(3697): 701–708.

Hildebrand M (1967) Symmetrical gaits of primates. *American Journal of Physical Anthropology* 26(2): 119–130.

Holmes P, Full RJ, Koditschek D, et al. (2006) The dynamics of legged locomotion: models, analyses, and challenges. *SIAM Review* 48(2): 207–304.

Hu DL, Nirody J, Scott T, et al. (2009) The mechanics of slithering locomotion. *Proceedings of the National Academy of Sciences* 106(25): 10081–10085.

Hwangbo J, Lee J, Alexey Dosovitskiy, et al. (2019) Learning agile and dynamic motor skills for legged robots. *Science Robotics* 4(26).

Jan Ijspeert A, Crespi A, Ryczko D, et al. (2007) From swimming to walking with a salamander robot driven by a spinal cord model. *Science* 315(5817): 1416–1420.

Jim Ostrowski and Joel Burdick (1998) The geometric mechanics of undulatory robotic locomotion. *The International Journal of Robotics Research* 17(7): 683–701.

Kafkafi N and Golani I (Jul 1998) A traveling wave of lateral movement coordinates both turning and forward walking in the ferret. *Biological Cybernetics* 78(6): 441–453. ISSN 1432-0770. DOI: 10.1007/s004220050448

Kohl N and Stone P (2004). Policy gradient reinforcement learning for fast quadrupedal locomotion. In IEEE International Conference on Robotics and Automation, 2004. Proceedings. ICRA'04. 2004, vol. 3. NY, USA, 2004, pp 2619–2624, IEEE.

Li J, Wang J, Yang SX, et al. (2016) Gait Planning and Stability Control of a Quadruped Robot. *Computational intelligence and neuroscience* 2016: 1–13.

Lin B, Chong B, Ozkan-Aydin Y, et al. (2020). Optimizing Coordinate Choice for Locomotion Systems with Toroidal Shape Spaces. In 2020 IEEE/RSJ International Conference on Intelligent Robots and Systems (IROS), NY, USA, 2020, p 7501–7506, IEEE. doi: 10.1109/IROS45743.2020.9341476

Maladen RD, Ding Y, Umbanhowar PB, et al. (2011) Undulatory swimming in sand: experimental and simulation studies of a robotic sandfish. *The International Journal of Robotics Research* 30(7): 793–805.

Marsden JE (1997) Geometric foundations of motion and control. In *Motion, Control, and Geometry: Proceedings of a Symposium, Board on Mathematical Science National Research Council Education*. Washington, DC: National Academies Press.

Marsden JE and TudorRatiu S (2013) *Introduction to mechanics and symmetry: a basic exposition of classical mechanical systems*. Springer Science & Business Media, vol. 17.

Marvi H, Gong C, Gravish N, et al. (2014) Sidewinding with minimal slip: snake and robot ascent of sandy slopes. *Science* 346(6206): 224–229.

McInroe B, Astley HC, Gong C, et al. (2016) Tail use improves performance on soft substrates in models of early vertebrate land locomotors. *Science* 353(6295): 154–158.

Murray RM (2017) *A Mathematical Introduction to Robotic Manipulation*. CRC Press.

Ramasamy S and Ross L (2016). Hatton. Soap-bubble optimization of gaits. In *2016 IEEE 55th Conference on Decision and Control (CDC)*, NY, USA, 2016, pages 1056–1062. IEEE.

Rieser JM, Gong C, Astley HC, et al. (2019) Geometric Phase and Dimensionality Reduction in Locomoting Living Systems. *arXiv preprint arXiv:1906.11374*. https://arxiv.org/abs/1906.11374

Schiebel PE, Astley HC, Rieser JM, et al. (2020) Mitigating memory effects during undulatory locomotion on hysteretic materials. *Elife* 9: e51412.

ScottKelly D and Murray RM (1995) Geometric phases and robotic locomotion. *Journal of Field Robotics* 12(6): 417–431.

Shapere A and Frank W (1989) Geometry of self-propulsion at low Reynolds number. *Journal of Fluid Mechanics* 198: 557–585.

Sharpe SS, Koehler SA, Kuckuk RM, et al. (2015) Locomotor benefits of being a slender and slick sand swimmer. *Journal of Experimental Biology* 218(3): 440–450.

Zhang T and Goldman DI (2014) The effectiveness of resistive force theory in granular locomotion a. *Physics of Fluids* 26(10): 101308.

Zhong B, Aydin YO, Gong C, et al. (2018) Coordination of back bending and leg movements for quadrupedal locomotion. In *Robotics: Science and Systems*.